


## Article

# Circularly Polarized Multiple-Input Multiple-Output Dielectric Resonator Antenna for 5G Millimeter-Wave Application

Ming Xu <sup>1</sup> and Jingwei Zhang <sup>1,2,\*</sup> <sup>1</sup> School of Science, Wuhan University of Technology, Wuhan 430070, China; 272984@whut.edu.cn<sup>2</sup> Sanya Science and Education Innovation Park of Wuhan University of Technology, Sanya 572000, China

\* Correspondence: j\_zhang@whut.edu.cn

**Abstract:** A circularly polarized (CP) multiple-input multiple-output (MIMO) dielectric resonator antenna (DRA) is presented in this paper for 5G millimeter-wave (mm-wave) applications. This MIMO antenna consists of two high-order mode CP DRAs, which use the modified cross slots to generate the CP fields. Two complementary split ring resonators (CSRR) are used to isolate the surface current on the metal ground, which can increase the antenna isolation and optimize the axial ratio when each port is excited. The proposed MIMO antenna obtains a simulated impedance bandwidth from 25.41 to 31.18 GHz and an axial ratio (AR) bandwidth (AR < 3 dB) from 25.49 to 29.52 GHz for the 5th generation wireless communication applications. The measured results show that the antenna covers the overlapped bandwidth of 11% and isolation less than −25 dB over the frequency band range. The measured average (peak) gain is 5.84 (6.24) dBic at 26.5 GHz to 29.5 GHz for port 1 and 6.90 (7.27) dBic for port 2.

**Keywords:** 5G communication; dielectric resonator antenna (DRA); multiple-input multiple-output (MIMO); millimeter-wave



**Citation:** Xu, M.; Zhang, J. Circularly Polarized Multiple-Input Multiple-Output Dielectric Resonator Antenna for 5G Millimeter-Wave Application. *Electronics* **2023**, *12*, 4258. <https://doi.org/10.3390/electronics12204258>

Academic Editor: Ikmo Park

Received: 12 September 2023

Revised: 6 October 2023

Accepted: 10 October 2023

Published: 15 October 2023



**Copyright:** © 2023 by the authors. Licensee MDPI, Basel, Switzerland. This article is an open access article distributed under the terms and conditions of the Creative Commons Attribution (CC BY) license (<https://creativecommons.org/licenses/by/4.0/>).

## 1. Introduction

As wireless communications evolve rapidly, the fifth generation (5G) communication technology is becoming of great importance due to its high-speed data transfer rates, low latency and high volume of traffic density [1]. According to the spectrum division, the 5G bands contain two parts: the Sub-6G band (450–6000 MHz) and the millimeter-wave band (24.25–52.6 GHz [2]. Due to the depletion of spectrum resources in the Sub-6G band, there is a growing focus on using the millimeter wave (mm-wave) band.

Several mm-wave antennas have been developed [3,4]. The antenna efficiency is degraded by the increasing ohmic losses and surface wave at mm-wave. DRAs have been investigated since the 1980's and are made of dielectric ceramic material with the advantages of no ohmic losses and extremely low dielectric losses, especially at high-frequency (mm-wave) [5]. Therefore, DRAs can reach very high radiation efficiency to be an ideal alternative antenna for a 5G millimeter-band wireless communication system.

MIMO technologies have been utilized for wireless communications, such as the 5G and potentially sixth generation of mobile systems, to improve channel capacity. Electromagnetic interference exists between the antenna elements in a compact MIMO system. The small element spacing leads to a stronger mutual coupling and interferences between antennas. Thus, high isolation is necessary in a MIMO system.

Recently, some MIMO DRA decoupling technology has been reported [6–9]. There are three main approaches to improve isolation in MIMO systems. One approach is to use filter structures, such as electromagnetic band-gaps (EBG) [10], metamaterials [11], and Frequency Selective Surfaces (FSSs) [12], interdicting surface current or electromagnetic (EM) waves between DRA elements. Another approach is loading metal parasitic strips [13] to constrain radiation E-fields inside DR to decrease mutual coupling between antennas.

The last approach uses specified higher-order modes [14] to improve isolation by exciting a negligibly weak field intensity upon the feeding wire of the coupling antenna. However, the approaches mentioned above are all focused on linearly polarized (LP) MIMO DRA, and only a few of them are designed for mm-wave applications.

Since the CP antenna can avoid polarization mismatch and maximize multipath attenuation, it is widely used in wireless communications. With the help of various feeding strategies [15–19] and specific DR geometry [20], circular polarization from DRAs can be obtained. Similar to the LP MIMO DRAs, the decoupling method in CP MIMO DRA is also attractive and highly concerned [21–23]. For instance, A cut-corner rectangular CP MIMO DRA with EBG is presented to operate from 3.15 to 3.8 GHz [21]. This design uses an irregular shape DR and an extra decoupling structure between two antennas, which increases the system complexity. In [22], eight striplines were added onto the surfaces of DR to reduce mutual coupling in CP MIMO Sub-6G application. However, this method may not be suitable for mm-wave because the mounted striplines increase the fabrication complexity and cost, especially on the micron scale. Due to the significant benefit of a high transmitting rate and communication stability, CP MIMO DRAs are required for mm-wave 5G communication systems. Currently, all designs for CP MIMO DRA are designed for Sub-6GHz and hardly extend their methods to mm-wave due to the design complexity. Thus, our work aims to investigate an mm-wave CP MIMO DRA with a traditional shape and low system complexity decoupling method.

In this article, a low-design complexity modified cross-fed CP DRA is proposed, and a CP MIMO antenna is also demonstrated for 5G mm-wave applications. The design improves the isolation by using a specific DR mode and two complementary split ring resonators (CSRR), which are applied to constrain surface waves on the metal ground to optimize the axial ratio when each of the two ports is excited. The measured impedance bandwidth of the antenna element is 25.1–31.09 GHz, and the axial ratio (AR) bandwidth are 25.3–26.0 (2.7%) and 27.2–29.8 (9.1%) GHz. The measured impedance bandwidth of the MIMO antenna is 25.32–31.76 GHz, and the axial ratio (AR) bandwidth is 26.70–30.00 (11.6%) GHz.

The organization of this work is as follows: The design and working mechanism of the CP DRA element, which is excited with high-order modes to improve the isolation in the MIMO antenna, is firstly described in Section 2. Then, the design process and the mechanism of the two-element MIMO DRA are explained in Section 3. Finally, in Section 4, the conclusions are given.

## 2. Antenna Element Design

The DRA MIMO system consists of left-handed CP DRA elements and two CSRRs. Subsequent subsections describe the design details and analysis of antenna elements and multiple-input multiple-output (MIMO) antenna systems.

### 2.1. CP DRA Element Configuration

Figure 1 shows the geometry of the proposed CP antenna element, which comprises a rectangular DR with the dimension  $a \times a \times h$  mounted on the 30 mm  $\times$  30.5 mm metal ground plane. The rectangular DR (Taizhou Wangling Insulation Materials Factory, TPA 615) with relative permittivity of 6.15 with a  $\tan \delta$  of 0.0016 is fitted on the Rogers 5880 substrate, which has a relative permittivity of 2.2 with a  $\tan \delta$  of 0.0009, and a thickness of 0.254 mm. The antenna is fed by a modified cross slot, which generates the resonant of DR and improves the Gain and CP properties of the antenna at operational bandwidth.

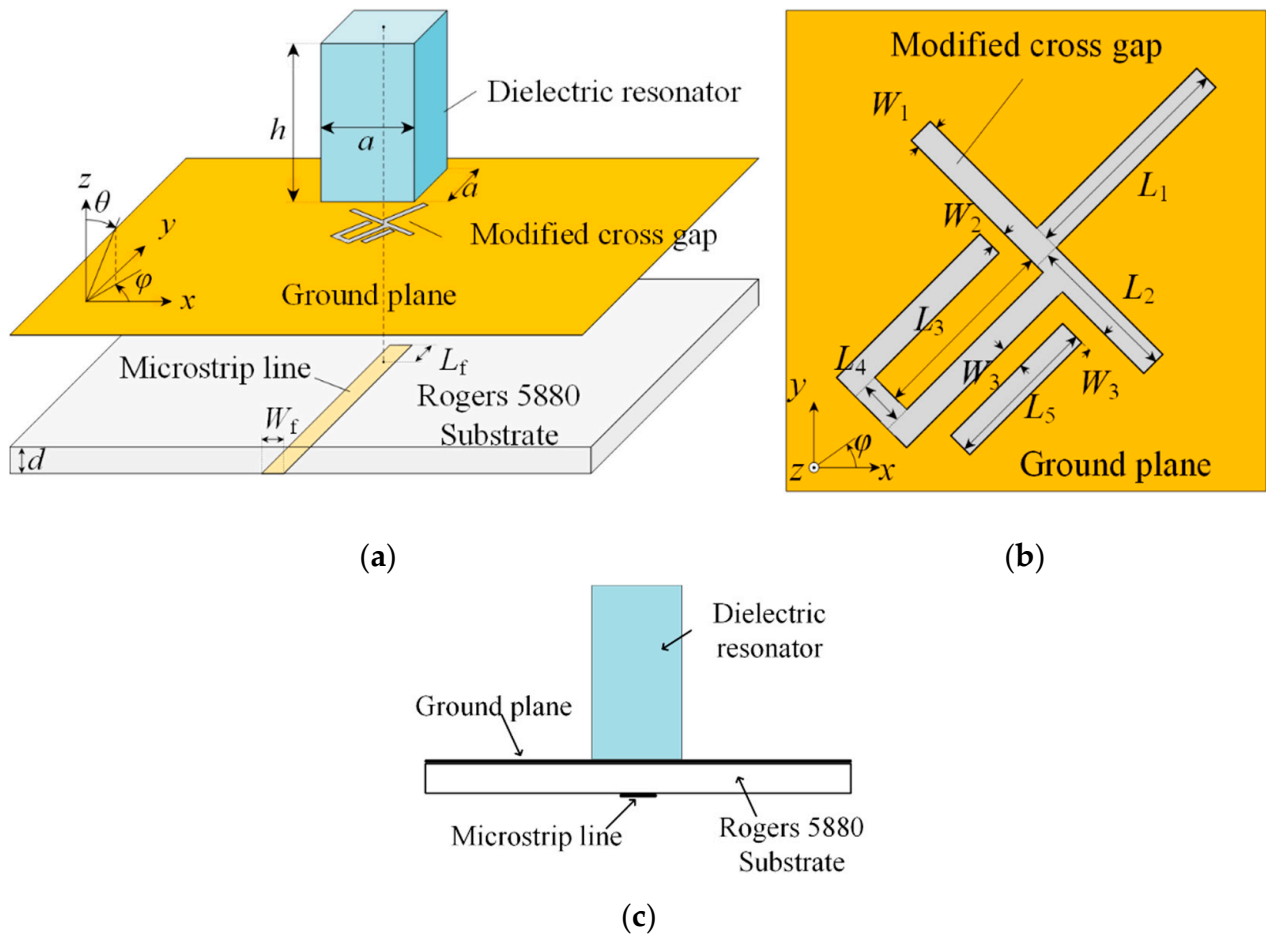


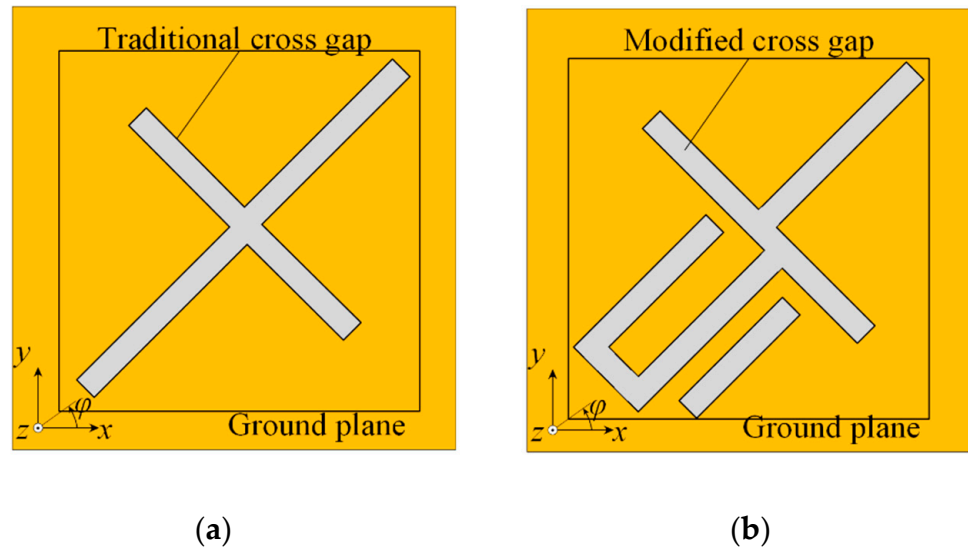
**Figure 1.** The configuration of the designed CP DRA: (a) perspectival view of the overall structure; (b) Overhead view of the modified cross gap; (c) the side view of the designed CP DRA.  $a = 3.2$ ;  $h = 5$ ;  $L_f = 1.8$ ;  $W_f = 0.76$ ;  $d = 0.254$ ;  $L_1 = 1.5$ ;  $L_2 = 1$ ;  $L_3 = 1.45$ ;  $L_4 = 0.24$ ;  $L_5 = 1.2$ ;  $W_1 = 0.15$ ;  $W_2 = 0.1$ ;  $W_3 = 0.1$ ; all in mm.

In an attempt to improve the isolation between antenna elements, the high-order mode  $TE_{\delta 13}^x$  and  $TE_{1\delta 3}^y$  are chosen to generate inside the DR. The number of standing waves generated by the rectangular DR in the  $x$ -axis,  $y$ -axis, and  $z$ -axis directions in different modes of operation is denoted by the subscripts  $m$ ,  $n$ , and  $p$ . The wave numbers  $k_x$ ,  $k_y$ , and  $k_z$  in the three directions inside the rectangular DR can be used to calculate the resonant frequency of the rectangular DR for the  $TE_{mnp}^x$  mode, respectively. By using Marcattili's approximation method [20], we can calculate the theoretical size of the DR at 27.5 GHz for the  $TE_{\delta 13}^x$  and  $TE_{1\delta 3}^y$  modes. After considering the effect of the End-Launch-Connector model, all the parameters are optimized in CST Microwave Studio, and the detailed parameters of the designed DRA are illustrated in Figure 1.

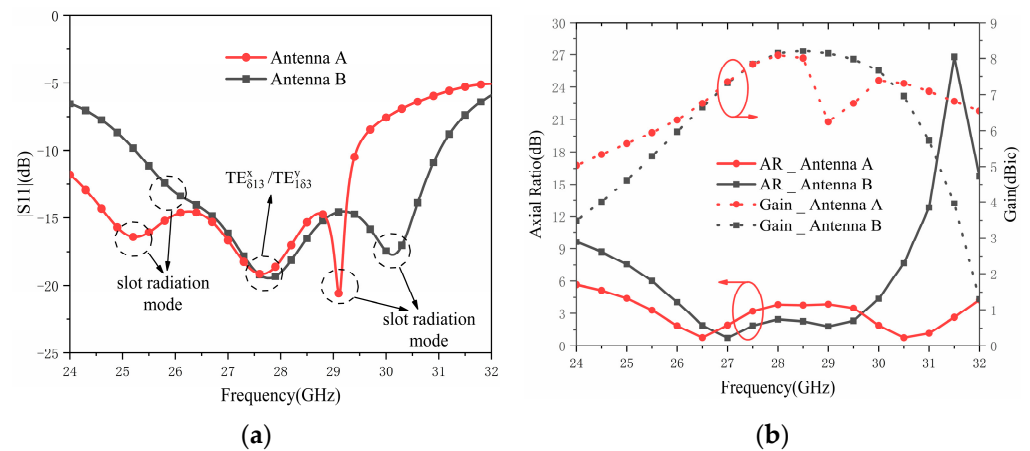
## 2.2. Working Mechanism

Figure 2 shows the configuration of two CP DRAs, which use the same DR but are fed by a traditional cross-feeding slot (Antenna A) and a modified cross-feeding slot (Antenna B). The AR is defined as the ratio of the major and minor axis of polarization ellipse transmitted or received by the antenna. In practice,  $AR < 3$  dB is used to define the polarization bandwidth or AR bandwidth. Since the slot-fed DRA is a hybrid antenna, the DR and slot are both resonant structures. The radiation performance is obtained by slot resonates and DR resonates. The simulated reflection coefficients ( $|S_{11}|$ ) and ARs for Antenna A and B are demonstrated in Figure 3. The DR resonant is obtained at 27.5 GHz

based on the conventional dielectric waveguide model. As shown in the results, Antenna A is recommended as the design starting point because of the wide impedance bandwidth (22.63–29.43 GHz) and its CP characteristics (25.64–27.44 GHz), which are obtained by high-order DR resonant modes ( $TE_{\delta 13}^x$  and  $TE_{1\delta 3}^y$ ) and slot resonant modes.



**Figure 2.** Feed structure of the DRA: (a) Antenna A (traditional cross gap); (b) Antenna B (modified cross gap).



**Figure 3.** Simulated results of Antenna A and B: (a)  $|S_{11}|$ ; (b) axial ratio and gain.

It is worth noting that in the DR mode, the slot is a feeding structure to excite the DR. While in the slot modes, the slot is a radiator, and the DR is a transmitting media. For a slot antenna, low radiating properties are mainly caused by the mismatching and the stored energy in the near field [24]. From Figure 3, it can be seen that Antenna A has a lower return loss than Antenna B at 29 GHz, but the gain of Antenna A is 2 dB lower than Antenna B. In addition, the result proves that both antennas match well at 29 GHz with an extremely small return loss. Therefore, the poor radiating capability is caused by the storage of near-field power. As shown in Figure 4a, Antenna A stores energy in the near field surrounding the slot and radiates weak power to the DR and open space. The consequences provide evidence that poor radiation capability and decreased gain at 29 GHz are due to radiation from the coupling slot. In order to release stored energy in the near field and improve radiating capability, a U-shaped modified cross slot is used in Antenna B. Figure 4b illustrates that the radiating capability of Antenna B is improved by increasing the effective power radiated away from the slots into the far field, which trend

to a higher gain. From simulated results, Antenna B obtained an impedance bandwidth ( $|S_{11}| < -10$  dB) of 25.23–31.02 GHz and an AR bandwidth ( $AR < 3$  dB) of 26.24–29.67 GHz. More importantly, the realized circular polarization gain of Antenna B at 29 GHz is much improved, as plotted in Figure 3b.

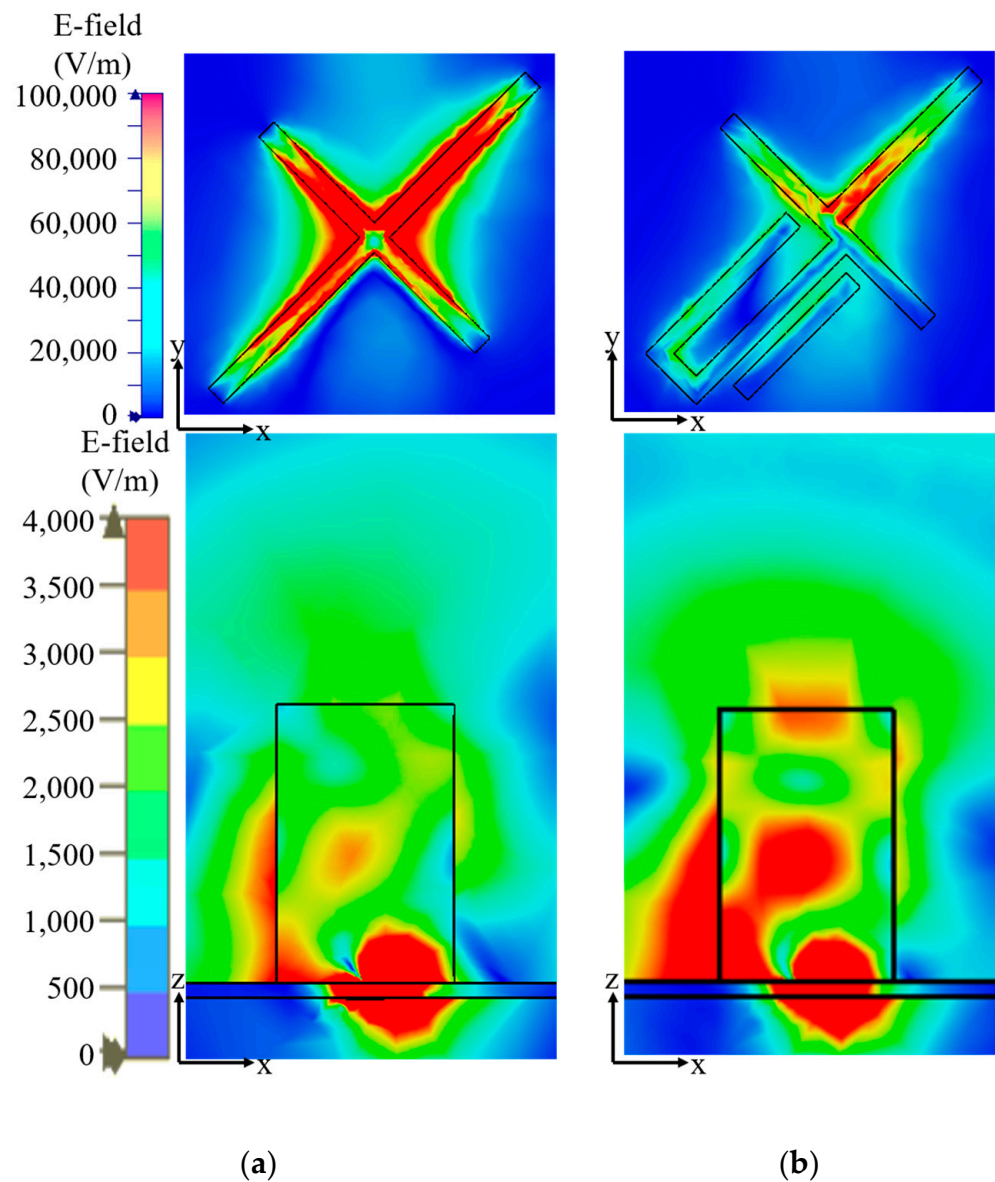


**Figure 4.** The distributions of the E-fields of Antenna A and B: (a) Antenna A (traditional cross gap); (b) Antenna B (modified cross gap).

Moreover, Figure 5 shows the E-field of the Antenna B at 28 GHz for a  $90^\circ$  phase difference. From the side view, it is obtained that the two orthogonal high-order modes  $TE_{\delta 13}^x$  and  $TE_{1\delta 3}^y$  are excited at 28 GHz, which is consistent with the theoretical results. From the top view, it is clear that at  $t = 0$  and  $t = T/4$  ( $T$  is the period), both E-fields have almost the same amplitude and rotate in the clockwise direction, which proves that the right-handed circular polarization (RHCP) is generated. In addition, Antenna B is a hybrid antenna in which the feeding slot works as a radiating part at 26.5 GHz. Figure 6 plots the E-field distribution of the slot to explain the operation mechanism of Antenna B. The vector  $\vec{E}_n$  represents the outcome vector of the localized E-field, where  $n = 1, 2, 3$ , and 4. The vector  $\vec{E}_R$  is the vector sum of the primary electric field vector  $\vec{E}_n$ . At 26.5 GHz,

the E-field is distributed at different locations of the cross slot at different moments, as shown in Figure 6, where  $\vec{E}_1$  to  $\vec{E}_4$  are the main local vectors of cross slot. It is obvious that  $\vec{E}_R$  are almost quadrature in direction and equal in magnitude at  $t = 0$  and  $t = T/4$ . This implies that the dielectric-loaded modified cross-slot antenna works in the RHCP. Thus, the combination of the modified cross slot and DR resonances produces a CP characteristic in this work.

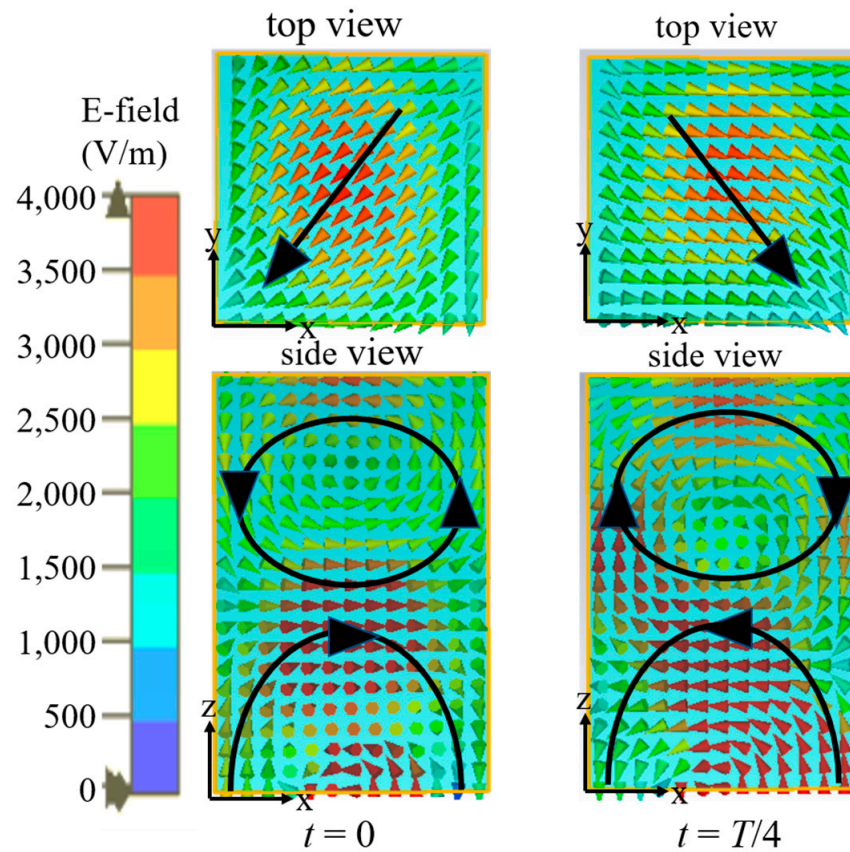


**Figure 5.** The distributions of the E-fields of DR at 28 GHz ( $t = 0$  and  $t = T/4$ ).

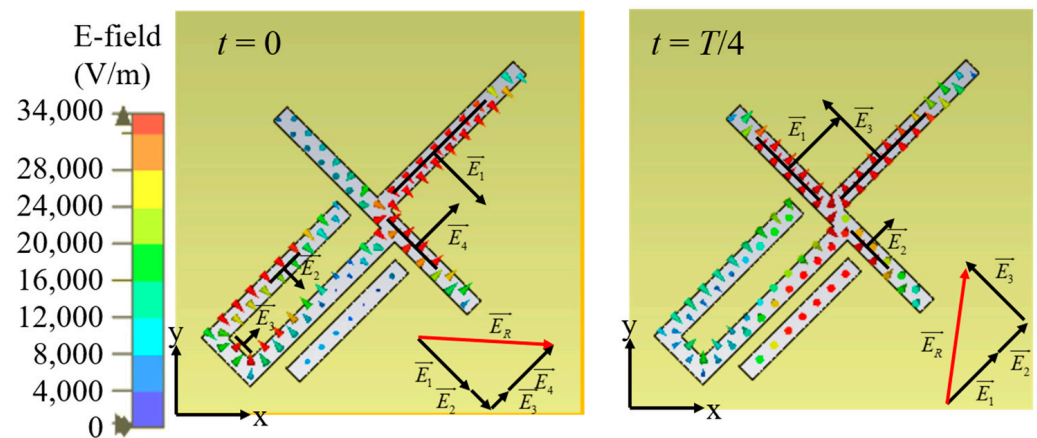


**Figure 6.** E-field distribution on the dielectric-loaded modified cross gap: 26.5 GHz at  $t = 0$  and  $t = T/4$ .

### 2.3. Parametric Study

A parametric study was performed using the CST MWS to investigate the proposed DRA. In this research, only one of the parameters was changed during the parametric scan. Two important parameters  $L_1$  and  $W_2$  is presented as follows.

Figure 7 demonstrates the simulated  $|S_{11}|$  and ARs of the designed DRA element with varied  $L_1$  values. As mentioned above, the slot resonance affects the impedance and AR bandwidth performance. From the results, the middle resonance almost stays fixed at 27.5 GHz, while the lower and upper resonance shifts down with increasing slot length due to the increase in the E-field on the long arm. It also provides evidence that the slot excites the upper and lower resonance. The E-field on the long arm of the slot becomes stronger with the increasing  $L_1$ , which also affects the primary E-field vector in the slot and indirectly affects the AR.

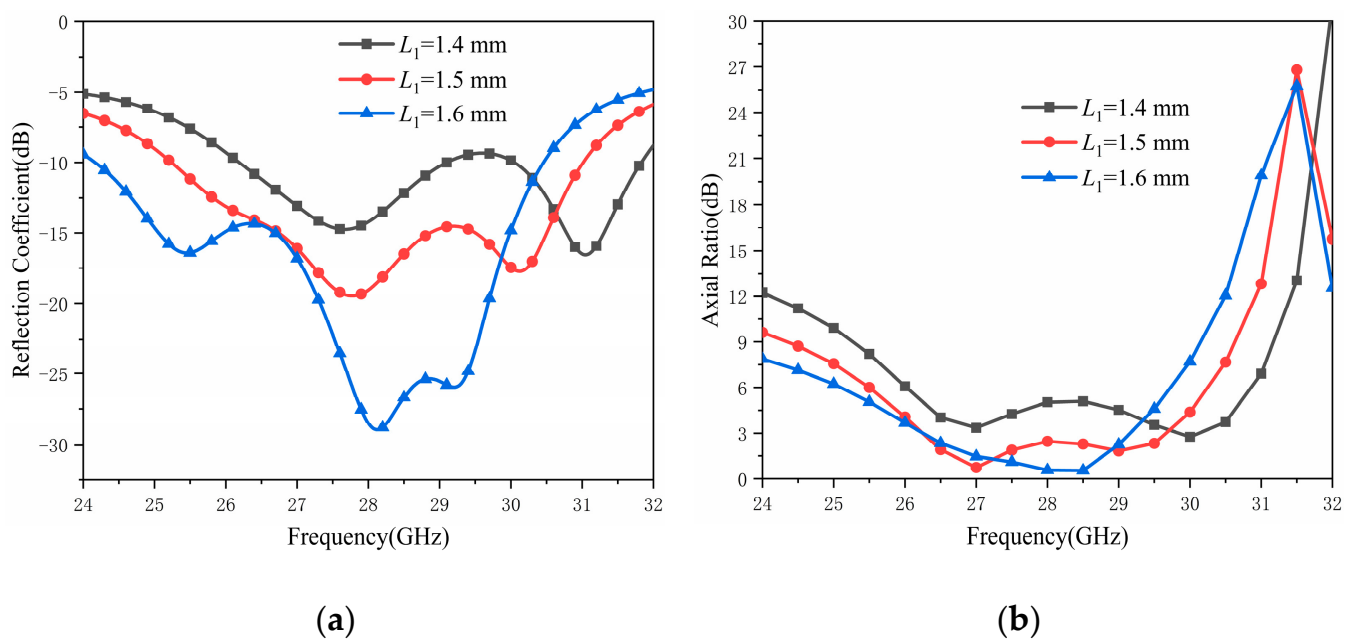
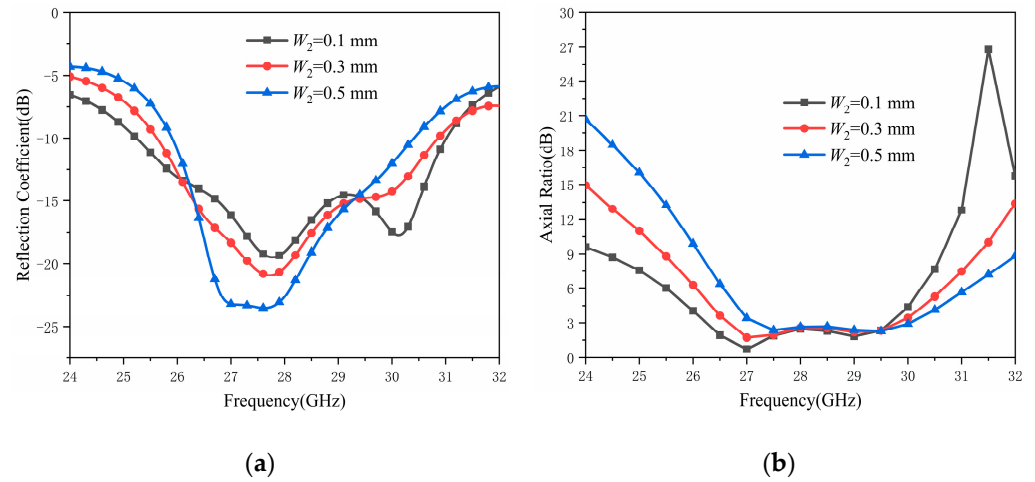


**Figure 7.** Simulated results of the CP DRA for slot with different  $L_1$ : (a)  $|S_{11}|$ ; (b) ARs.

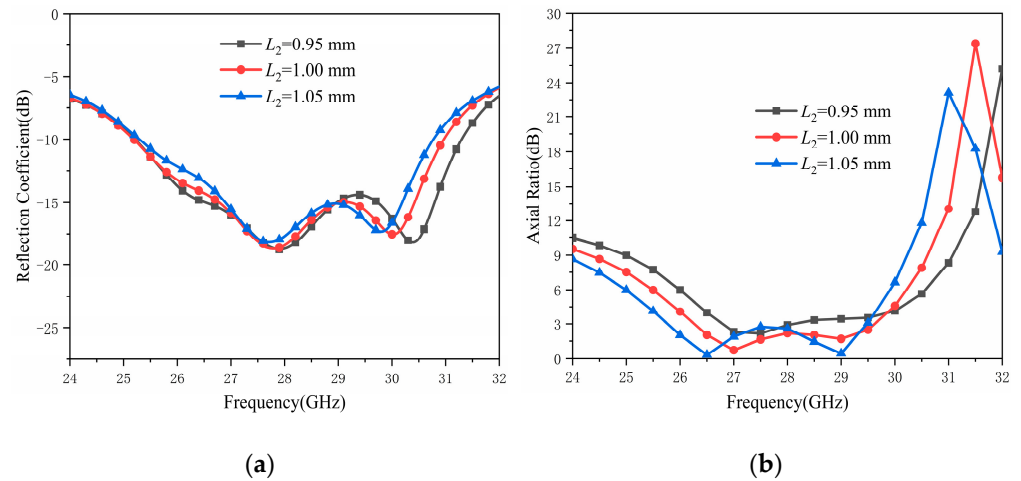
Figure 8 illustrates the simulated  $|S_{11}|$  and ARs of the designed DRA with varied  $W_2$  values. As  $W_2$  decreases, both impedance and AR bandwidths of the designed antenna at the first slot resonance frequency (around 27 GHz) are shifted downward due to the increase in the coupling between the current in the short arm of the cross slot and the current in the long arm.

Figure 9 displays the simulated  $|S_{11}|$  and ARs of the designed DRA element with varied  $L_2$  values. As mentioned above, slot resonance has less effect on the impedance and mainly affects the AR bandwidth performance. From the results, the antenna impedance bandwidth does not change significantly as  $L_2$  increases, and the AR of the designed antenna is shifted downward at the first slot resonance frequency (around 27 GHz) and the second slot resonance frequency (around 29 GHz).

In addition to the above structural parameters, other parameters also have little effect on regulating the performance of dielectric resonator antenna, such as  $L_f$  on the impedance matching having a regulatory role on the axis ratio has little effect.



**Figure 8.** Simulated results of the CP DRA for slot with different  $W_2$ : (a)  $|S_{11}|$ ; (b) ARs.



**Figure 9.** Simulated results of the CP DRA for slot with different  $L_2$ : (a)  $|S_{11}|$ ; (b) ARs.

#### 2.4. Measurement Results

A CP DRA element was designed, fabricated, and measured to demonstrate its performance. The photograph is inserted in Figure 10. An end-launch-connector of 1.85-KFD0830 manufactured by Gwave, Inc. (Beijing, China) was connected to the microstrip feedline, and the DR was attached to the ground plane using an adhesive purchased from TONSAN, Inc. (Beijing, China). For reflection coefficient measurement, the test antenna was directly connected to a calibrated VNA (Agilent E5072A). Based on the measurement method presented in [25], axial ratio, gain, and radiation patterns are tested in anechoic chamber. In the measurement system, a rectangular horn worked as the source antenna and the antenna under test was placed on the turntable. The measured AR can be calculated as follows.

$$E_{LHCP} = \frac{1}{\sqrt{2}} \{ [H_A \cos(H_P) + V_A \sin(V_P)] + j[H_A \sin(H_P) - V_A \cos(V_P)] \} \quad (1)$$

$$E_{RHCP} = \frac{1}{\sqrt{2}} \{ [H_A \cos(H_P) - V_A \sin(V_P)] + j[H_A \sin(H_P) + V_A \cos(V_P)] \} \quad (2)$$

$$AR = 20 \log \left| \frac{|E_{LHCP}| + |E_{RHCP}|}{|E_{LHCP}| - |E_{RHCP}|} \right| \quad (3)$$

where  $H_A$  and  $V_A$  are the horizontal and vertical amplitude measured with the source orientated at  $0^\circ$  and  $90^\circ$ , and  $H_P$  and  $V_P$  are the phase of horizontal and vertical components. Figure 10 shows the measured and simulated reflection coefficient of the proposed element. The measured impedance bandwidth ( $|S_{11}| < -10$  dB) of the element is 25.23 to 31.02 GHz, which covers the 5G mm-wave application. The measured ARs bandwidth ( $AR < 3$  dB) covers 25.3–26.0 (2.7%) and 27.2–29.8 (9.1%) GHz. The measured CP gain is also illustrated, and the average (peak) gain is 7.51 (7.95) dBic at 26.5 GHz to 29.5 GHz. The simulated impedance bandwidth and realized gain roughly agree with the measured result. The differences between simulated and measured AR results at 2.7 GHz are mainly caused by the unavoidable air gap between the media block and the metal floor, the dielectric constant changes during the fabrication process of composite ceramic TPA 615, and the slot tolerance. It is also worth noting that the placement and support during the antenna measurement in the anechoic chamber affects the radiation pattern, leading to a possibly high AR [26]. Figure 11 gives the measured and simulated radiation patterns at 26 GHz and 29 GHz. It is shown that the DRA element has a broadside unidirectional radiation pattern at two frequencies, producing RHCP in the +z direction.

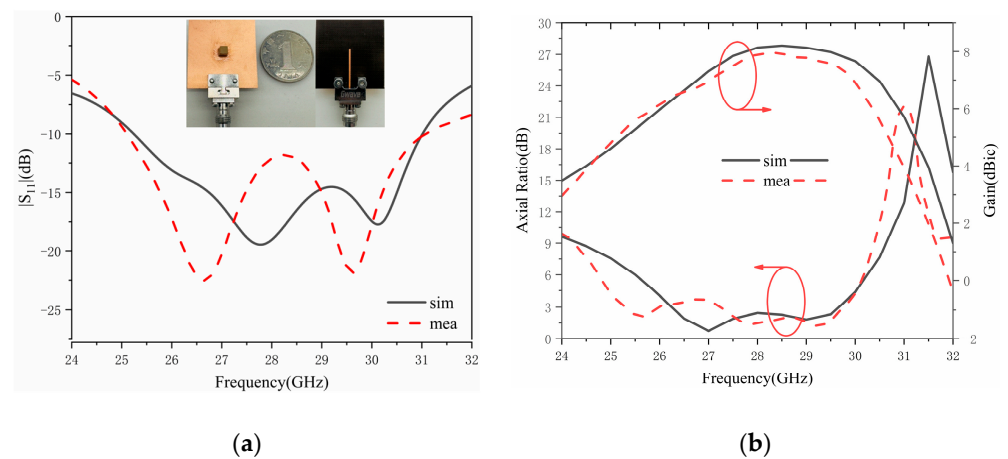


**Figure 10.** Simulated and measured results of the designed CP DRA element: (a)  $|S_{11}|$ ; (b) ARs and Gains.

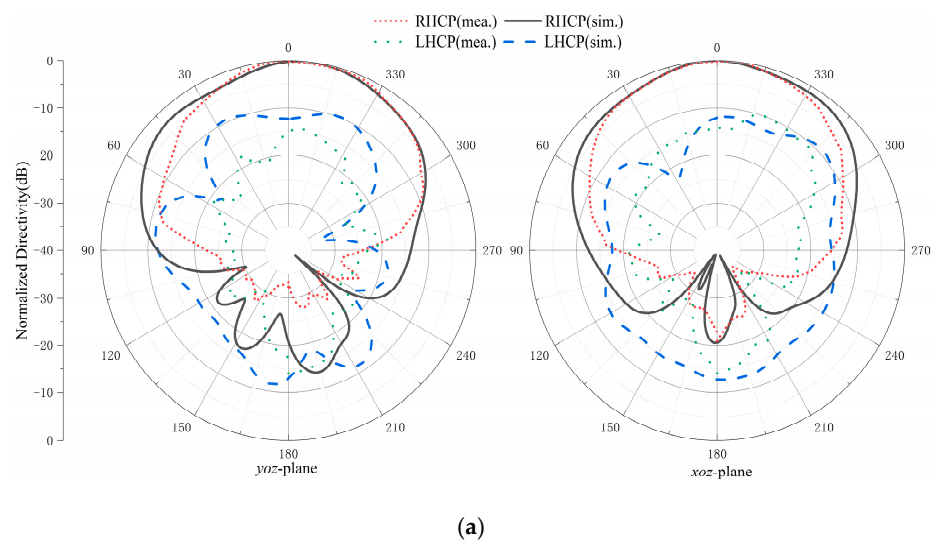


**Figure 11.** Cont.

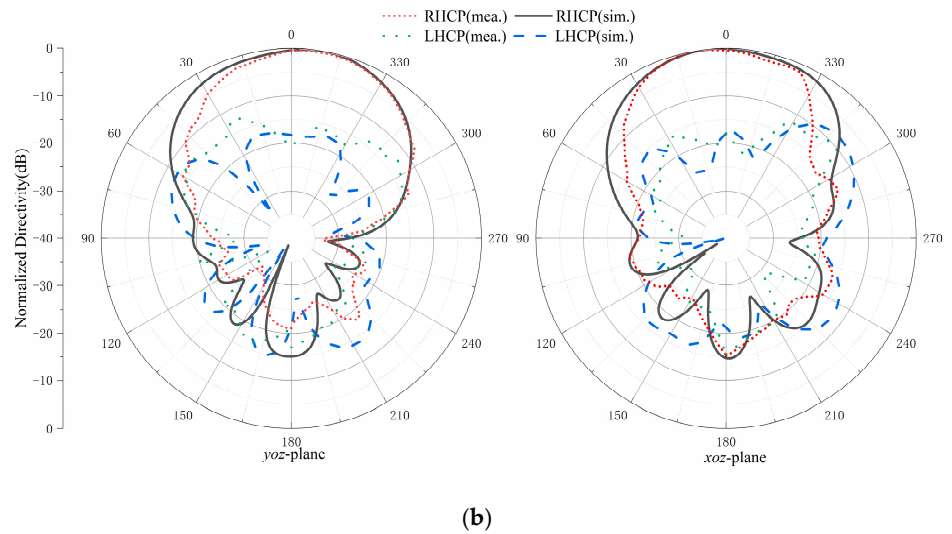
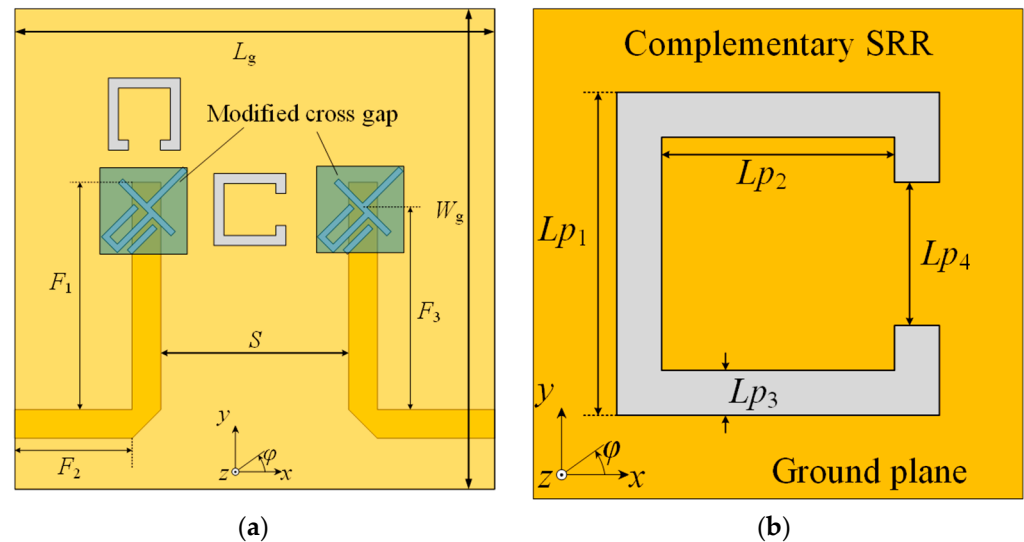


**Figure 11.** Measured and simulated radiation patterns of the designed CP DRA element: (a) at 26 GHz; (b) at 29 GHz.

### 3. CP MIMO Antenna Design

#### 3.1. MIMO Configuration

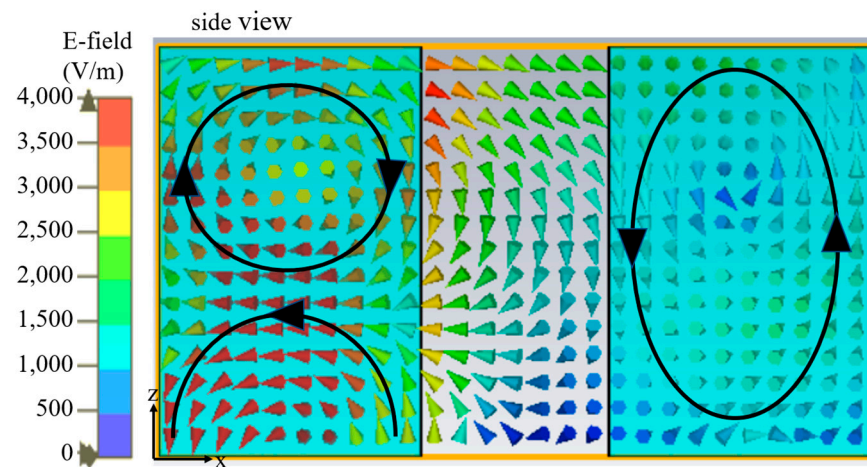
Figure 12 shows the configuration of the designed CP MIMO antenna. This design uses two DRA elements proposed above and two complementary split ring resonators (CSRRs) that are etched on the ground plane to isolate the surface waves on the metal ground, which can increase the antenna isolation, improve diversity performance, and optimize the axial ratio when each of the two ports is excited. All the optimized parameters are illustrated in Figure 12.



**Figure 12.** The designed CP MIMO DRA configuration: (a) overhead view of the whole structure; (b) overhead view of the modified cross gap.  $L_g = 27.5$ ;  $W_g = 30$ ;  $F_1 = 6.04$ ;  $F_2 = 10.62$ ;  $F_3 = 4.24$ ;  $L_{p1} = 2.1$ ;  $L_{p2} = 1.15$ ;  $L_{p3} = 0.33$ ;  $L_{p4} = 0.76$ ;  $S = 5.5$  ( $0.48\lambda$ ); all in mm.

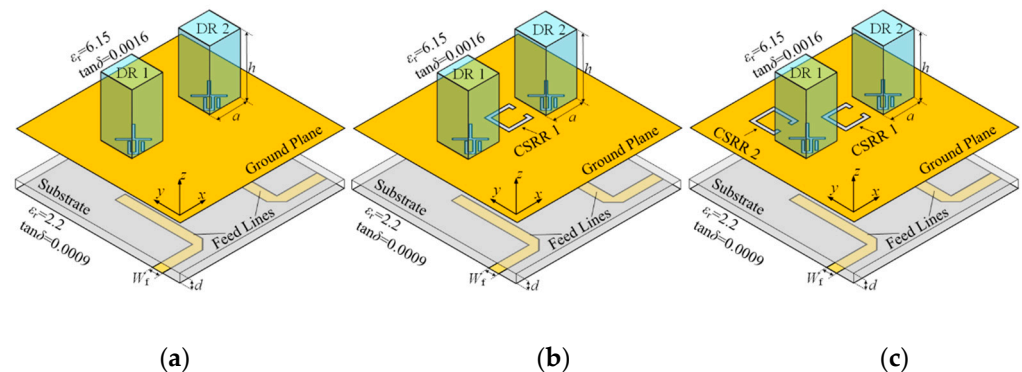
Due to generating a proper high-order mode, the mutual coupling between DRs has been suppressed. Take  $T = 0$  as an example, Port 1 excited a  $TE_{\delta 13}^x$  mode in DR1, a coupled  $TE_{\delta 12}^x$  mode is generated in DR2 with a weak field intensity, as shown in Figure 13. As we know, due to the boundary condition of the DRA, the  $TE_{\delta 12}^x$  mode is unable to be coupled

to port 2. Thus, the high isolation between two DRs is achieved. Notably, the proposed DRA element is a hybrid antenna, so we also need to decrease the coupling between slots.

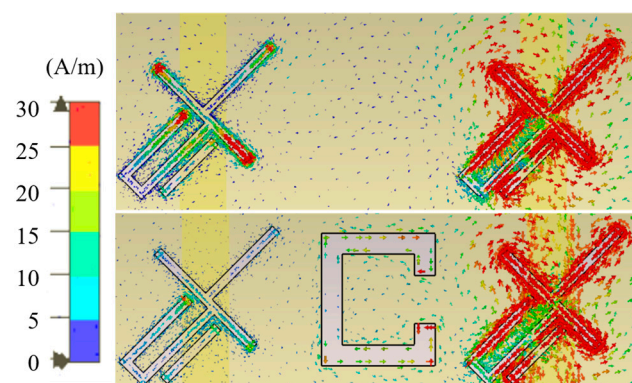


**Figure 13.** The E-field distribution inside the MIMO DRA at 28 GHz.

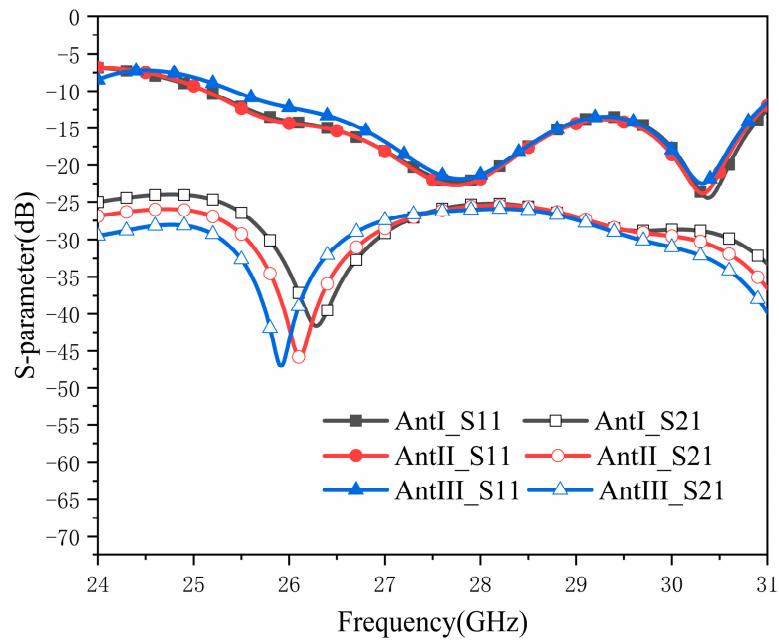
Figure 14 shows the layout of three CP MIMO DRA with and without CSSR. The CSSRs shown in Figure 14c are used to constrain the surface current (in Figure 15) on the ground plane at 26 GHz (slot mode), which can improve the antenna isolation (in Figure 16). It is also obtained that at 26 GHz, the CSRR1 added in the center of the two DRs improves the AR as port 2 works, and CSRR2 above DR1 improves the AR as port 1 works.



**Figure 14.** The configuration of designed CP MIMO DRA: (a) Ant I; (b) Ant II; (c) Ant III (designed).

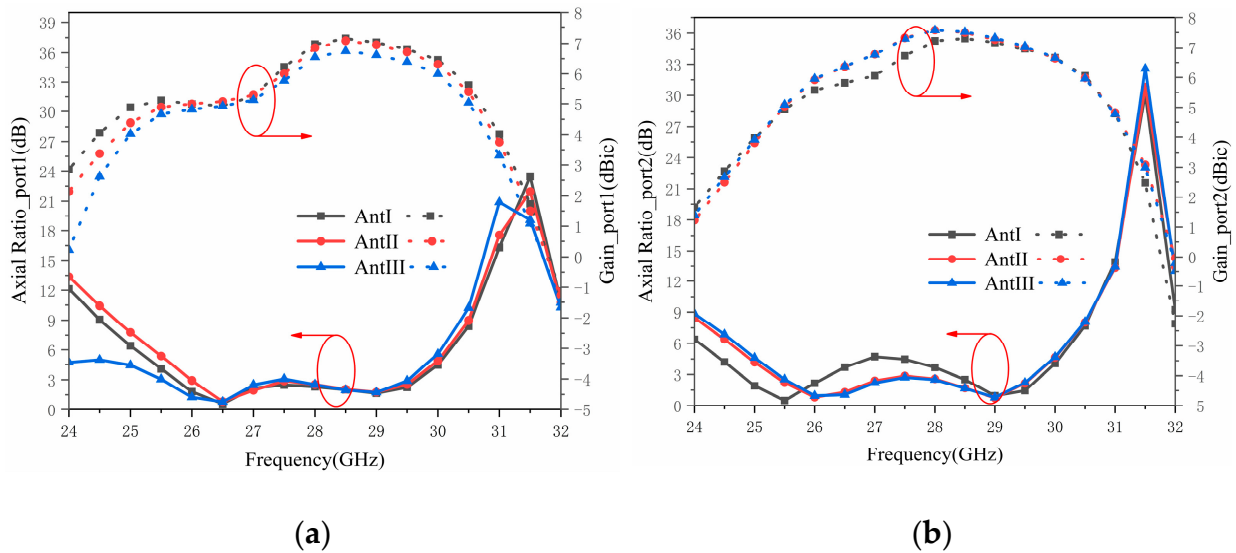


**Figure 15.** The surface current on the plane of grounding at 26 GHz.



**Figure 16.** Simulated S-parameter for the three reference antennas.

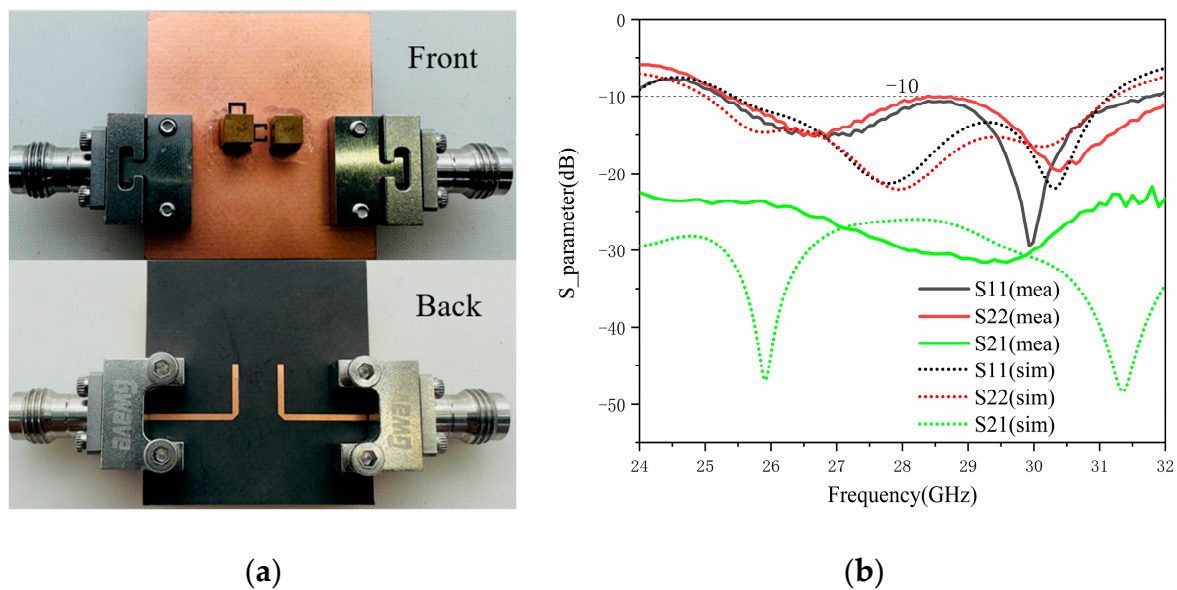
It can be obtained that the impedance bandwidth covers 25.37–31.15 GHz, and that  $|S_{21}|$  is less than  $-26$  dB at operational bandwidth. Figure 17 shows the simulated axial ratio and realized circular polarization gain. It is clear that the AR bandwidth was obtained from 25.49 to 29.52 GHz and, a maximum gain of 6.74 dBic for port 1 and 7.61 dBic was obtained for port 2 in the bandwidth.



**Figure 17.** Simulated gains and ARs of the three reference MIMO antenna: (a) when port1 works; (b) when port2 works.

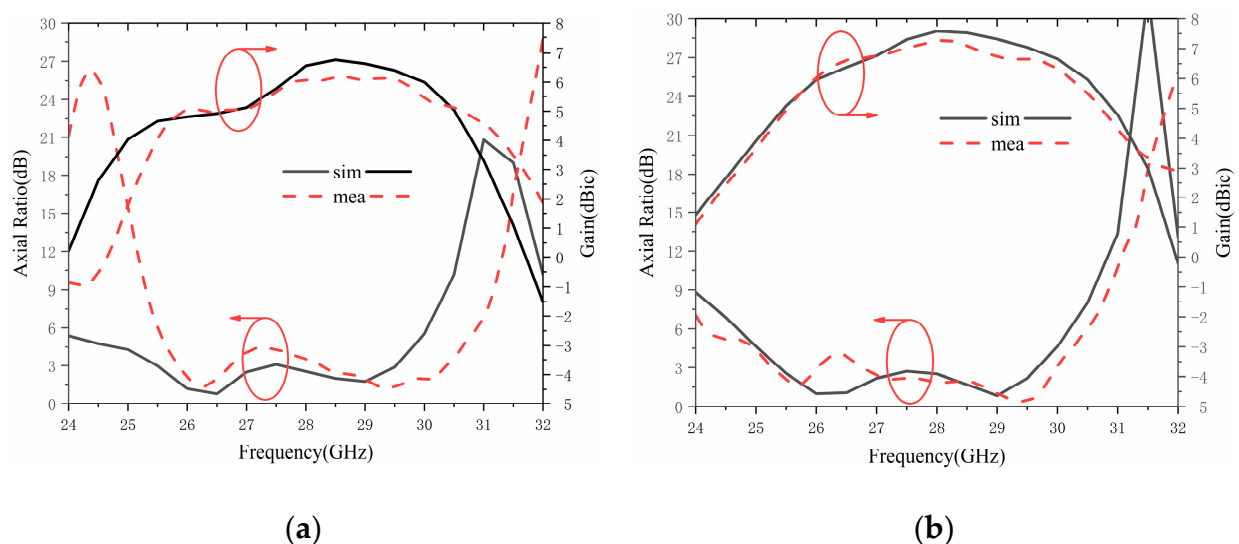
### 3.2. Antenna Radiation Performance

Figure 18 reports the measured and simulated S-parameters results of the proposed MIMO DRA. The measured  $|S_{11}|$  bandwidth of the designed CP MIMO DRA range from 25.25 to 31.76 GHz and  $|S_{22}|$  bandwidth range from 25.32 to 32.00 GHz, which covers the desire frequency. The measured isolation for  $|S_{21}| > 25$  dB is achieved over the required bandwidth.



**Figure 18.** (a) Structure of the designed CP MIMO DRA, (b) and measured and simulated S-Parameter of the designed CP MIMO DRA.

From Figure 19, the measured ARs are lower than 3 dB over 25.80–26.80 (3.8%) and 28.2–30.4 (7.5%) when port 1 works and 25.20–26.10 (3.5%) and 26.70–30.00 (11.6%) when port 2 works. Due to the fabrication errors mentioned in Section 2.3, the simulation results slightly differ from the measured results. Figure 19 shows the measured, simulated circularly polarized gain. The measured average (peak) gain is 5.77 (6.19) dBic at 26.5 GHz to 29.5 GHz when port 1 works and 6.90 (7.27) dBic when port 2 works. The measured and simulated radiation patterns at 26 GHz and 29 GHz are shown in Figure 20. The DRA has a broadside unidirectional radiation pattern at two frequencies, producing RHCP in the +z direction.



**Figure 19.** Measured and simulated gains and ARs of the designed CP MIMO antenna: (a) port 1 works; (b) port 2 works.

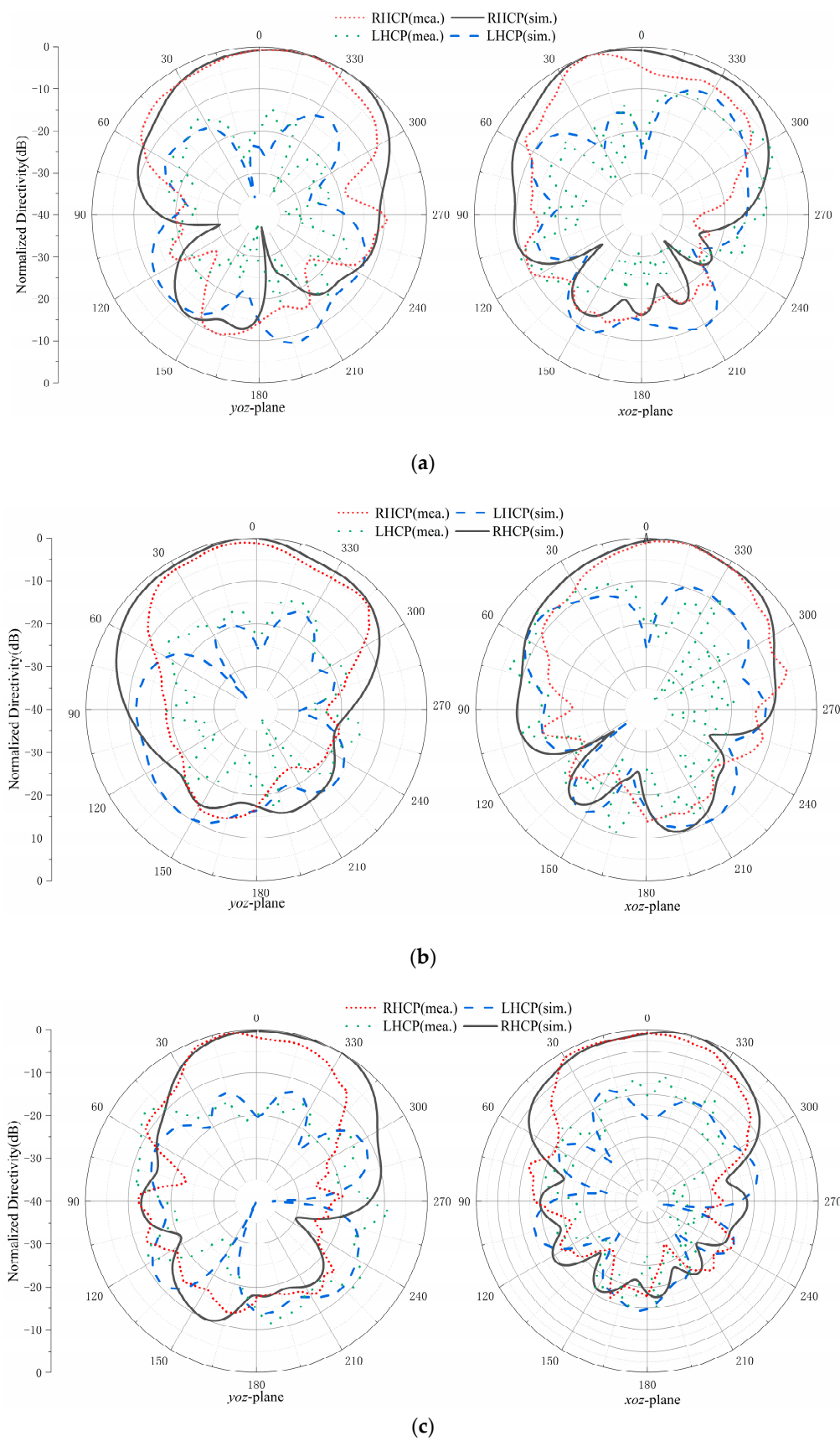
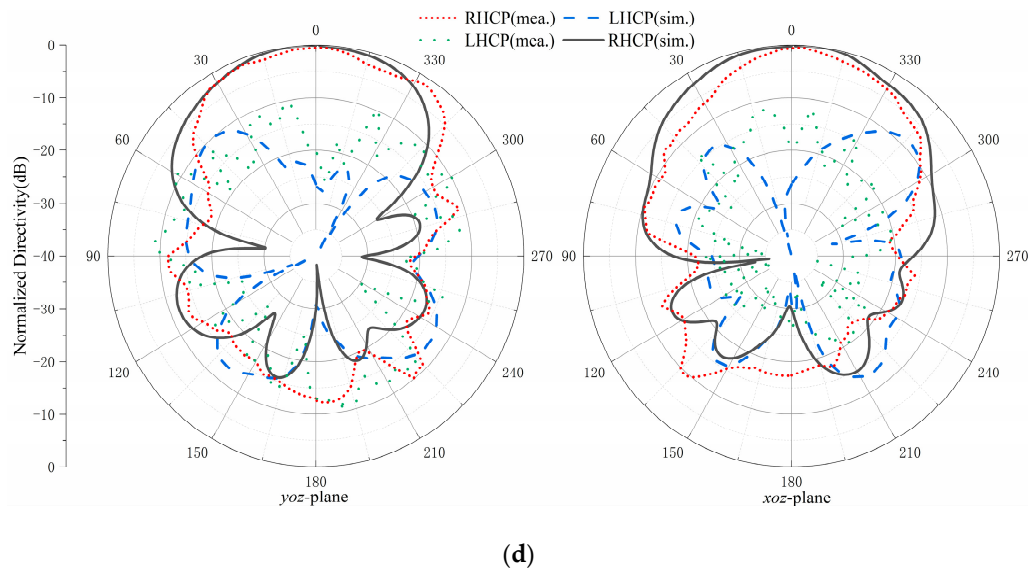


Figure 20. Cont.



**Figure 20.** Measured and simulated radiation patterns of the designed CP MIMO antenna: (a) radiation patterns at 26 GHz when port 1 works; (b) radiation patterns at 26 GHz when port 2 works; (c) radiation patterns at 29 GHz when port 1 works; (d) radiation patterns at 29 GHz when port 2 works.

### 3.3. Diversity Performance

The Envelope Correlation Coefficient (ECC) is utilized to characterize the correlation between the individual elements of a MIMO antenna. Diversity Gain (DG) can be calculated by the ECC. A higher DG and smaller ECC can be obtained using multiple radiation patterns or decoupling in a singular plane. The simulated values of ECC and DG for the entire operating band are illustrated in Figure 21. The simulated ECC value is less than 0.0005, and the calculated DG value is better than 9.9975, which is very suitable for mm-wave wireless applications. The ECC of the broadband MIMO antenna is calculated using Equation (4). The DG of the broadband MIMO antenna is calculated using Equation (5).

$$\rho_{ij} = \frac{\left| \iint_{4\pi} \bar{F}_i(\theta, \phi) \cdot \bar{F}_j^*(\theta, \phi) d\Omega \right|^2}{\iint_{4\pi} |\bar{F}_i(\theta, \phi)|^2 d\Omega \cdot \iint_{4\pi} |\bar{F}_j(\theta, \phi)|^2 d\Omega} \quad (4)$$

$$DG = 10 \sqrt{1 - ECC^2} \quad (5)$$

where  $\bar{F}_i(\theta, \phi)$  is the three-dimensional field pattern of the antenna at the  $i$ th port of excitation,  $\Omega$  is the steradian angle measured on a spherical plane, and the symbol \* stands for conjugate.

Table 1 displays the comparisons of the designed MIMO DRA with other related works. It is clear that the designed mm-wave MIMO DRA has a CP with a smaller ECC and a higher isolation. In addition, the proposed MIMO DRA uses a rectangular DR with specified resonate modes and CSRRs to improve isolation, which has lower design complexity. This is also the first time a CP MIMO DRA has been implemented in the mm-wave band.

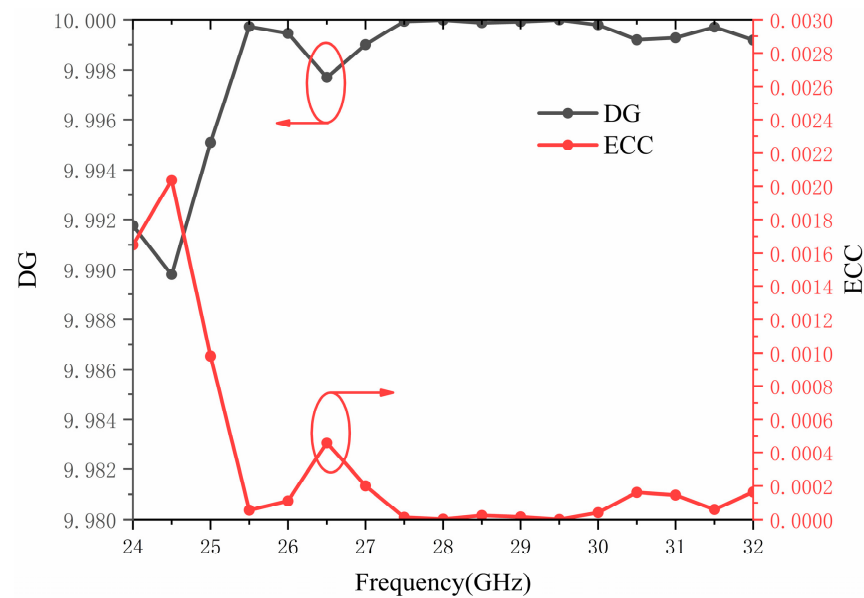


Figure 21. Simulated ECC and DG of the designed CP MIMO DRA.

Table 1. Comparison of the performance of the designed DRA with the MIMO DRAs reported previously.

Ref. No.	Working Bands	Polarization Method	Design Complexity	3-dB AR Bandwidth (GHz)	Decoupling Methods	Size of DRAs (mm <sup>3</sup> )	ECC
[14]	Sub-6G	LP	Low	NA	specified modes	$0.24 \times 0.24 \times 0.36 \lambda_0^3$	NA
[22]	Sub-6G	CP	High	4.9%	metal parasitic strips	$0.23 \times 0.23 \times 0.14 \lambda_0^3$	$\leq 0.006$
[23]	Sub-6G	CP	High	13.23%	orthogonal feed	$0.92 \times 0.92 \times 0.16 \lambda_0^3$	$\leq 0.05$
[21]	Sub-6G	CP	High	18.7%	EBG	$0.21 \times 0.21 \times 0.23 \lambda_0^3$	$\leq 0.03$
[12]	Mm-wave	LP	High	NA	FSS	$0.2 \times 0.2 \times 0.24 \lambda_0^3$	$\leq 5 \times 10^{-6}$
[13]	Mm-wave	LP	Medium	NA	metal parasitic strips	$0.67 \times 0.88 \times 0.24 \lambda_0^3$	$\leq 0.013$
Proposed work	Mm-wave	CP	Low	11.6%	specified modes and CSRR	$0.3 \times 0.3 \times 0.47 \lambda_0^3$	$\leq 0.0005$

$\lambda_0$ : Free-space wavelength at the center frequency.

#### 4. Conclusions

In this article, a hybrid CP DRA element is designed for 5G mm-wave applications using the modified cross-fed slot and high-order DR modes. In addition, a two-element MIMO antenna is designed, fabricated, and tested. In the MIMO antenna, two CSRRs are used to isolate the surface waves on the metal ground, increasing the antenna isolation and optimizing the axial ratio when each of the two ports is excited. The proposed wide beamwidth CP MIMO antenna obtains a measured peak gain of 7.2 dBic and overlapped bandwidth of 11%, which covers the 5G applications.

**Author Contributions:** J.Z.: Conceptualization, supervision and project administration, analysis data, writing and editing manuscript; M.X.: investigation and design, data analysis and experiment, writing and editing the manuscript. All authors have read and agreed to the published version of the manuscript.

**Funding:** This research was supported by the Fundamental Research Funds for the Central Universities (Grant No.: WUT 2021IVB029), the Open Funds for Sanya Science and Education Park (Grant No. 2021KF0018), and the National Natural Science Foundation of China (Grant No.: 62001338).

**Data Availability Statement:** Data sharing not applicable. No new data were created or analyzed in this study. Data sharing is not applicable to this article.

**Conflicts of Interest:** The authors declare no conflict of interest.

## References

1. Rappaport, T.S.; Xing, Y.; MacCartney, G.R.; Molisch, A.F.; Mellios, E.; Zhang, J. Overview of millimeter wave communications for fifth-generation (5G) wireless networks-With a focus on propagation models. *IEEE Trans. Antennas Propag.* **2014**, *32*, 1065–1082. [\[CrossRef\]](#)
2. Hong, W.; Jiang, Z.H.; Yu, C.; Hou, D.; Wang, H.; Guo, C.; Hu, Y.; Kuai, L.; Yu, Y.; Jiang, Z.; et al. The role of millimeter-wave technologies in 5G/6G wireless communications. *IEEE J. Microw.* **2021**, *7*, 101–122. [\[CrossRef\]](#)
3. Qiu, H.; Liu, H.; Jia, X.; Jiang, Z.Y.; Liu, Y.H.; Xu, J.; Lu, T.; Shao, M.; Ren, T.-L.; Chen, K.J. Compact, flexible, and transparent antennas based on embedded metallic mesh for wearable devices in 5G wireless network. *IEEE Trans. Antennas Propag.* **2021**, *69*, 1864–1873. [\[CrossRef\]](#)
4. Jilani, S.F.; Alomainy, A. A multiband millimeter-wave 2-D array based on enhanced franklin antenna for 5G wireless systems. *IEEE Antennas Wirel. Propag. Lett.* **2017**, *16*, 2983–2986. [\[CrossRef\]](#)
5. Ng, H.; Leung, K. Dielectric resonator antennas. In *Encyclopedia of RF and Microwave Engineering*; John Wiley & Sons, Inc.: Hoboken, NJ, USA, 2003.
6. Sahu, N.K.; Das, G.; Gangwar, R.K. Dual polarized triple-band dielectric resonator based hybrid MIMO antenna for WLAN/WiMAX applications. *Microw. Opt. Technol. Lett.* **2018**, *60*, 1033–1041. [\[CrossRef\]](#)
7. Kang, L.; Li, H.; Wang, X.; Shi, X. Compact offset microstrip-fed MIMO antenna for band-notched UWB applications. *IEEE Antennas Wirel. Propag. Lett.* **2015**, *14*, 1754–1757. [\[CrossRef\]](#)
8. Sharma, A.; Das, G.; Gangwar, R.K. Dual polarized triple band hybrid MIMO cylindrical dielectric resonator antenna for LTE2500/WLAN/WiMAX applications. *Int. J. RF Microw. Comput. Aided Eng.* **2016**, *26*, 763–772. [\[CrossRef\]](#)
9. Das, G.; Sahu, N.K.; Sharma, A.; Gangwar, R.K.; Sharawi, M.S. FSS-based spatially decoupled back-to-back four-port MIMO DRA with multidirectional pattern diversity. *IEEE Antennas Wirel. Propag. Lett.* **2019**, *18*, 1552–1556. [\[CrossRef\]](#)
10. Mu’Ath, J.; Denidni, T.A.; Sebak, A.R. Millimeter-wave compact EBG structure for mutual coupling reduction applications. *IEEE Trans. Antennas Propag.* **2015**, *63*, 823–828.
11. Dadgarpour, A.; Zarghooni, B.; Virdee, B.S.; Denidni, T.A.; Kishk, A.A. Mutual coupling reduction in dielectric resonator antennas using metasurface shield for 60 GHz MIMO systems. *IEEE Antennas Wirel. Propag. Lett.* **2017**, *16*, 477–480. [\[CrossRef\]](#)
12. Karimian, R.; Kesavan, A.; Nedil, M.; Denidni, T.A. Low-mutual-coupling 60 GHz MIMO antenna system with frequency selective surface wall. *IEEE Antennas Wirel. Propag. Lett.* **2017**, *16*, 373–376. [\[CrossRef\]](#)
13. Zhang, Y.; Deng, J.Y.; Li, M.J.; Sun, D.; Guo, L.X. A MIMO dielectric resonator antenna with improved isolation for 5G millimeter-wave applications. *IEEE Antennas Wirel. Propag. Lett.* **2019**, *18*, 747–751. [\[CrossRef\]](#)
14. Pan, Y.M.; Hu, Y.; Zheng, S.Y. Design of low mutual coupling dielectric resonator antennas without using extra decoupling element. *IEEE Trans. Antennas Propag.* **2021**, *69*, 7377–7385. [\[CrossRef\]](#)
15. Yang, M.; Pan, Y.; Yang, W. A singly fed wideband circularly polarized dielectric resonator antenna. *IEEE Antennas Wirel. Propag. Lett.* **2018**, *17*, 1515–1518. [\[CrossRef\]](#)
16. Huang, R.; Zhang, J.; Zhang, C. Dual-Band Circularly Polarized Hybrid Dielectric Resonator Antenna for 5G Millimeter-Wave Applications. *Electronics* **2022**, *11*, 1761. [\[CrossRef\]](#)
17. Li, B.; Hao, C.X.; Sheng, X.Q. A dual-mode quadrature-fed wideband circularly polarized dielectric resonator antenna. *IEEE Antennas Wirel. Propag. Lett.* **2009**, *8*, 1036–1038.
18. Yang SL, S.; Chair, R.; Kishk, A.A.; Lee, K.F.; Luk, K.M. Study on sequential feeding networks for subarrays of circularly polarized elliptical dielectric resonator antenna. *IEEE Trans. Antennas Propag.* **2007**, *55*, 321–333. [\[CrossRef\]](#)
19. Movahedinia, R.; Sebak, A.R.; Chaharmir, M.R.; Nikkhah, M.R.; Kishk, A.A. X-band circularly polarized electronically steerable parasitic array radiator of DRA. *IEEE Trans. Antennas Propag.* **2018**, *66*, 721–728. [\[CrossRef\]](#)
20. Lu, L.; Jiao, Y.C.; Zhang, H.; Wang, R.; Li, T. Wideband circularly polarized antenna with stair-shaped dielectric resonator and open-ended slot ground. *IEEE Antennas Wirel. Propag. Lett.* **2016**, *15*, 1755–1758. [\[CrossRef\]](#)
21. Chen, H.N.; Song, J.M.; Park, J.D. A compact circularly polarized MIMO dielectric resonator antenna over electromagnetic band-gap surface for 5G applications. *IEEE Access* **2019**, *7*, 140889–140898. [\[CrossRef\]](#)
22. Hu, Y.; Pan, Y.M.; Di Yang, M. Circularly Polarized MIMO Dielectric Resonator Antenna with Reduced Mutual Coupling. *IEEE Trans. Antennas Propag.* **2021**, *69*, 3811–3820. [\[CrossRef\]](#)
23. Sahu, N.K.; Das, G.; Gangwar, R.K. Dielectric resonator-based wide band circularly polarized MIMO antenna with pattern diversity for WLAN applications. *Microw. Opt. Technol. Lett.* **2018**, *60*, 2855–2862. [\[CrossRef\]](#)
24. Buerkle, A.; Sarabandi, K.; Mosallaei, H. Compact slot and dielectric resonator antenna with dual-resonance, broadband characteristics. *IEEE Trans. Antennas Propag.* **2005**, *53*, 1020–1027. [\[CrossRef\]](#)

25. Toh, B.Y. Understanding and Measuring Circular Polarization. *IEEE Trans. Educ.* **2003**, *46*, 313–318.
26. Yin, J.Y.; Wan, X.; Ren, J.; Cui, T.J. A circular polarizer with beamforming feature based on frequency selective surfaces. *Sci. Rep.* **2017**, *7*, 41505. [[CrossRef](#)] [[PubMed](#)]

**Disclaimer/Publisher's Note:** The statements, opinions and data contained in all publications are solely those of the individual author(s) and contributor(s) and not of MDPI and/or the editor(s). MDPI and/or the editor(s) disclaim responsibility for any injury to people or property resulting from any ideas, methods, instructions or products referred to in the content.